

A HYDRODYNAMICAL SOLUTION FOR THE “TWIN-TAILED” COLLIDING GALAXY CLUSTER “EL GORDO”

SANDOR. M. MOLNAR¹ & TOM BROADHURST^{2,3}

Draft version February 29, 2024

ABSTRACT

The distinctive cometary X-ray morphology of the recently discovered massive galaxy cluster “El Gordo” (ACT-CT J0102-4915; $z = 0.87$) indicates that an unusually high-speed collision is ongoing between two massive galaxy clusters. A bright X-ray “bullet” leads a “twin-tailed” wake, with the SZ centroid at the end of the Northern tail. We show how the physical properties of this system can be determined using our FLASH-based, N-body/hydrodynamic model, constrained by detailed X-ray, Sunyaev–Zel’dovich (SZ), and Hubble lensing and dynamical data. The X-ray morphology and the location of the two Dark Matter components and the SZ peak are accurately described by a simple binary collision viewed about 480 million years after the first core passage. We derive an impact parameter of $\simeq 300$ kpc, and a relative initial infall velocity of $\simeq 2250$ km s⁻¹ when separated by the sum of the two virial radii assuming an initial total mass of $2.15 \times 10^{15} M_{\odot}$ and a mass ratio of 1.9. Our model demonstrates that tidally stretched gas accounts for the Northern X-ray tail along the collision axis between the mass peaks, and that the Southern tail lies off axis, comprising compressed and shock heated gas generated as the less massive component plunges through the main cluster. The challenge for Λ CDM will be to find out if this physically extreme event can be plausibly accommodated when combined with the similarly massive, high infall velocity case of the Bullet cluster and other such cases being uncovered in new SZ based surveys.

Subject headings: galaxies: clusters: general – galaxies: clusters: individual (ACT-CT J0102-4915) – galaxies: clusters: intracluster medium – methods: numerical

1. INTRODUCTION

Collisions between galaxy clusters are the most energetic events in the cosmos, with unique implications for structure-formation and the nature of dark matter. The concordance Λ CDM model, predicts that the infall velocities of massive merging systems are typically less than 1000 km s⁻¹ (Thompson & Nagamine 2012). However, a few massive merging clusters discovered recently suggest a significant tail in the velocity distribution at high infall velocities ($\gtrsim 3000$ km s⁻¹). The Bullet cluster (1E0657-56) is readily identified as an extreme example by its clearcut Mach cone found in its X-ray image (Markevitch et al. 2002). Velocities derived from X-ray observations using the shock jump conditions and N-body/hydrodynamical simulations support this interpretation (Mastropietro & Burkert 2008; Springel & Farrar 2007; Markevitch et al. 2004), but with inferred velocities in the range 2700–4500 km s⁻¹. Several other merging clusters have been subsequently found with a bullet-cluster-like morphology (A2744: Owers et al. 2012; A2146: Russel et al. 2010), and some also identified as high-infall-velocity systems (CL J0152-1347: using detailed hydrodynamical simulations; Molnar et al. 2012; MACS J0717.5+3745: using radial velocities and the kinematic SZ effect; Sayers et al. 2013; Mroczkowski et al. 2012). These high-infall-velocity merging clusters provide a potential challenge for the concordance Λ CDM model. However, to test the concordance model with these mergers, we need more accurate and robust determination of impact velocities based on multifrequency observations and detailed numerical simulations, as well as

larger volume cosmological simulations to define the probability of these extreme merging systems (Watson et al. 2014; Thompson & Nagamine 2012).

The newly discovered “El Gordo” galaxy cluster (ACT-CL J0102-4915, $z = 0.87$) by the Atacama Cosmology Telescope (ACT) Sunyaev–Zel’dovich (SZ) cluster survey (Marriage et al. 2011) has the largest SZ decrement of any cluster reported and displays a bullet-like X-ray morphology in deep follow-up Chandra images (Menanteau et al. 2012). Multifrequency observations of this cluster show a large offset between the X-ray and SZ centroids, and between the X-ray and the centroid of mass-surface density of the main cluster component (Zitrin et al. 2013; Jee et al. 2013). These large offsets are simple distinguishing features caused by high velocity encounters as shown by Molnar et al. (2012) using N-body/hydrodynamical simulations, suggesting that El Gordo is a high-infall-velocity merging cluster. The lensing work identified El Gordo as the most massive cluster known at $z \gtrsim 0.6$, as of today (Jee et al. 2013; Menanteau et al. 2012).

In this paper we present results from numerical simulations of idealized binary encounters between galaxy clusters containing dark matter and gas initially in equilibrium based on the adaptive mesh code, FLASH. Our main goal is to find a physical interpretation of the overall features of El Gordo found in multifrequency observations. The structure of this paper is the following. In Section 2 we summarize results from previous analyses of El Gordo based on multifrequency observations and numerical simulations. Then, in Section 3, we describe our FLASH simulations, and methods to obtain simulated X-ray and SZ images, and mass surface density maps. We present our results and provide a physical interpretation of the morphology of multifrequency observations of El Gordo in Section 4. We discuss our results in comparison with previous investigations in Section 5. We summarize our findings and their implications to cosmology in Section 6.

¹ Department of Physics, National Taiwan University, Taipei 10617, Taiwan, sandor@phys.ntu.edu.tw

² Department of Theoretical Physics, University of the Basque Country, Bilbao 48080, Spain

³ Ikerbasque, Basque Foundation for Science, Alameda Urquijo, 36-5 Plaza Bizkaia 48011, Bilbao, Spain

Unless stated otherwise, errors quoted are 68% CL. We adopt, as our concordance cosmological model, the 5-year WMAP cosmology, $\Omega_m = 0.23$, $\Omega_\Lambda = 0.73$, and $H_0 = 70.50 \text{ km s}^{-1} \text{ Mpc}^{-1}$ (Komatsu et al. 2009). This model gives the scaling of $1'$ corresponds to 459.5 kpc (note, we do not use the dimensionless Hubble parameter, h , because numerical simulations work with physical distances).

2. MULTI-FREQUENCY OBSERVATIONS OF EL GORDO

El Gordo has the largest SZ decrement in the 455 deg² ACT SZ cluster survey (Marriage et al. 2011), and the most significant detection in the overlapping 2500 deg² South Pole Telescope (SPT) Sunyaev-survey (Williamson et al. 2011). It was confirmed as a high redshift ($z = 0.870$) galaxy cluster by optical observations (Menanteau et al. 2012, 2010). The amplitude of the SZ decrement of El Gordo is comparable to the massive Bullet cluster, and it was found to be the most massive, X-ray, and SZ right cluster at $z \gtrsim 0.6$ discovered as of today (Menanteau et al. 2012).

A detailed study of this cluster using multifrequency observations was presented by Menanteau et al. (2012). Chandra ACIS-I observations of El Gordo reveal a disturbed morphology. The X-ray emission of the cluster is elongated in the South–East to North–West direction. One of the tails is following the peak emission at an angle of about 45° towards North-West (Northern tail), below that is located the Southern tail, which may be interpreted as a wake from a merging event. Menanteau et al. found a high overall X-ray temperature of $T_X = 14.5 \pm 0.1 \text{ keV}$, and a peak temperature of $\sim 20 \text{ keV}$ around the shock region. Based on the X-ray morphology, the high X-ray temperature and SZ amplitude, Menanteau et al. suggested that El Gordo is a high-infall-velocity binary merger at high redshift, very similar to the Bullet cluster located at a lower redshift.

The relative positions of the mass surface density, the X-ray and SZ peaks are important in the physical interpretation of a merging galaxy cluster such as El Gordo. Menanteau et al. (2012) located two main peaks in the images of the galaxy number density, the rest frame i -band and $3.6 \mu\text{m}$ luminosity density, and stellar mass density (derived from infrared IRAC/Spitzer imaging using a spectral energy distribution fitting procedure), which are correlated with the mass distribution. They concluded that the NW mass component centered on the Northern tail is more massive than the mass center in the SE, in the vicinity of the X-ray peak. The SZ peak was found to be close to the NW component slightly offset toward the SE component. Their results suggest a mass ratio of about 2:1 of the two components. Based on the cometary morphology, the high X-ray temperature, the mass distribution, and the offsets between mass peaks and the X-ray and SZ peaks, Menanteau et al. suggest that the bright X-ray peak marks the emission from an infalling cluster moving from the NW towards SE plunging through the main cluster disrupted in its X-ray emission indicating a large infall velocity producing a wake with two tails.

Using mass scaling relations based on X-ray, SZ observations and velocity dispersion, Menanteau et al. (2012) estimated a total virial mass of El Gordo to be $1.51 \pm 0.22 \times 10^{15} h^{-1} M_\odot$. They found that all of their mass estimates are less than 2σ away from the interval of $1.2\text{--}2.0 \times 10^{15} h^{-1} M_\odot$. This mass estimate for El Gordo is compatible with subsequent analyses of strong and weak lensing data: $1.6 \times 10^{15} h^{-1} M_\odot$ (Zitrin et al. 2013), and $2.15 \times 10^{15} h^{-1} M_\odot$ (Jee et al. 2013),

respectively.

Based on the X-ray morphology and that the location of the peak of the galaxy number distribution of the SE component which precedes the X-ray peak by $173 h^{-1} \text{ kpc}$, Menanteau et al. suggest that El Gordo is a high redshift close analogue to the bullet cluster. In this scenario, as a consequence of the high infall velocity, the gas (marked by the X-ray peak) trails the dark matter associated with the infalling cluster (marked by the peak of the galaxy number distribution) due to ram pressure. However, this close analogy with the bullet cluster is questionable, because another mass proxy, the peak of the i -band luminosity and the mass peak of the infalling cluster from weak lensing (Jee et al. 2013) are, in fact, trailing the X-ray peak. The positions of the mass peaks estimated using different methods scatter around the X-ray peak within a 173 kpc, thus we conclude that the offset between the X-ray peak and the center of the infalling cluster has not been established.

Recently discovered massive high redshift clusters and large impact velocity merging clusters pose a potential challenge to the concordance ΛCDM model (Thompson & Nagamine 2012; Lee & Komatsu 2010). Menanteau et al. (2012) and Jee et al. (2013) estimated the probability to find a cluster with the mass and the redshift of El Gordo based on cosmological numerical simulations using the exclusion curve method of Mortonson, Hu & Huterer (2011), and concluded that, although a cluster such as El Gordo is a rare massive cluster, it is within the allowed mass range predicted by the ΛCDM models. However, Jee et al. (2013) noted that a more accurate mass measurement may put El Gordo into the excluded region.

The discovery of the Bullet cluster with its high inferred infall velocity provided the first challenge to the concordance ΛCDM model (Mastropietro & Burkert 2008). Estimates based on cosmological simulations found that the probability of finding a cluster with the infall velocity implied by the bullet cluster is very unlikely (Thompson & Nagamine 2012; Lee & Komatsu 2010; Hayashi & White 2006). Thompson & Nagamine (2012) used cosmological simulations with different box sizes ($0.25\text{--}2 h^{-1} \text{ Gpc}$) to improve the accuracy of the probability distribution at the high end of the velocity tail taking into account the effect of the box size. They confirmed that it is very unlikely (3×10^{-8}) to find even one massive cluster merger with impact velocity of $\gtrsim 3000 \text{ km s}^{-1}$ in a concordance ΛCDM model at the redshift of the Bullet cluster. The most probable infall velocity was found to be about 550 km s^{-1} , (see Figure 15 of Thompson & Nagamine 2012). Most recently Watson et al. (2014) carried out a simulation using large box size ($6 h^{-1} \text{ Gpc}$) to improve on the statistics of large clusters and rare cosmological events. They found no merging system with the same large relative velocity, spatial separation, and redshift as the Bullet cluster (see their Figure 7). They conclude, however, that this might be due to their low statistics of these rare major mergers at a fixed redshift. Clearly, more numerical work is necessary to quantify the probability distribution of relative velocities of mergers as a function of redshift, masses, and distances between the components.

Since the discovery of the Bullet cluster several other merging clusters have been found with large offsets between the X-ray peak and the SZ and dark matter surface density peaks (MACS J0025.4-1222: Bradač et al. 2008; CL J0152-1347: Massardi et al. 2010; A2163: Bourdin et al. 2011; MACS J0744.8+3927 and CL J1226.9+3332: Korngut et al. 2011;

MACS J0717.5+3745: Mroczkowski et al. 2012; DLSCL J0916.2+2951: Dawson et al. 2012; SL2S J08544-0121: Gastaldello et al. 2014). These offsets are generated by the different behavior of the collisionless component, the dark matter, and the gas during the merging process: the dark matter responds only to gravity, but the gas is subject to hydrodynamical effects, and that the X-ray emission and the SZ effect depend differently on the gas density and temperature.

The size of the offsets between the dark matter and the gas peaks is determined by the relative strength of the gravitational force which is trying to keep the gas locked into the potential well of the dark matter, and the ram pressure which is removing gas from the infalling subcluster. Using N/body–hydrodynamical simulations of merging galaxy clusters, Molnar et al. (2012) showed that a large impact velocity is necessary to explain hundreds of kpc scale offsets.

The relative velocity of El Gordo was estimated by Menanteau et al. (2012) from the measured line-of-sight peculiar velocity difference between the SE and NW galaxy concentrations, as $586 \pm 96 \text{ km s}^{-1}$. However, for the BCG, they found a higher velocity difference: $731 \pm 66 \text{ km s}^{-1}$. Assuming a projection angle relative to the plane of the sky of θ , the relative velocity can be expressed as $586/\sin\theta$. Based on the X-ray morphology, Menanteau et al. argue that θ should be small, and they obtain a relative velocity of 2300 km s^{-1} and 1200 km s^{-1} assuming 15° and 30° for θ , and use this to estimate the infall velocity. The location of radio relics ahead and behind the two mass centers enclosed by the detected X-ray emission support this interpretation (Lindner et al. 2014). These estimated infall velocity values fall on the less likely to the unlikely region of the velocity probability distribution derived by Thompson & Nagamine (2012). Menanteau et al. conclude that a more accurate determination of the infall velocity is necessary for El Gordo using numerical simulations to find out whether it is allowed by the concordance Λ CDM model.

Binary merger simulations to reproduce the observed properties of El Gordo using a publicly available smoothed particle hydrodynamics (SPH) code GADGET-3 (Springel 2005; Dolag & Stasyszyn 2009) was carried out by Donnert (2014). The parameters of the initial setup were based on those derived by Menanteau et al. (2012). Donnert (2014) reproduced the X-ray luminosity of El Gordo and the observed distances between the peaks of the dark matter surface density distribution and X-ray emission and SZ effect. However, the X-ray morphology has not been reproduced well: the leading X-ray peak followed only by one tail close to the collision axis (the line connecting the two dark matter centers). Donnert is suggesting that the reason why the two-tailed X-ray morphology was not reproduced was the lack of substructure in the simulation.

3. FLASH SIMULATIONS FOR EL GORDO

We carried out self-consistent numerical simulations of binary galaxy cluster mergers including dark matter and intra-cluster gas using the publicly available Eulerian parallel code, FLASH, developed at the Center for Astrophysical Thermonuclear Flashes at the University of Chicago (Fryxell et al. 2000 and Ricker 2008). FLASH, with its new modules, offers the possibility for the future to include many non-gravitational processes, such as thermal conduction, viscosity, radiative cooling, and magnetohydrodynamics, which might be relevant for certain aspects of cluster merging. The box size of our simulations was 13.3 Mpc on a side, reaching the high-

est resolution, i.e., cell size, of 12.7 kpc at the merger shocks and the centers of the clusters. Our simulations were semi-adiabatic, i.e., only shock heating was included. In order to establish our notation and for the convenience of the reader, we briefly summarize our well established simulation method here, a detailed description and verifications of the method can be found in Molnar et al. (2013a,b, 2012).

3.1. Initial setup

As initial conditions for the two colliding clusters, for the distribution of the dark matter and the intracluster gas, we assumed spherical models with a cut off at the virial radius of each cluster ($r \leq R_{\text{vir}}$). We adopted a NFW model (Navarro, Frenk & White 1997) for the dark matter distribution:

$$\rho_{DM}(r) = \frac{\rho_s}{x(1+x)^2}, \quad (1)$$

where $x = r/r_s$, and ρ_s , $r_s = R_{\text{vir}}/c_{\text{vir}}$ are scaling parameters for the density and radius, and c_{vir} is the concentration parameter. We assumed a truncated non-isothermal β model for the gas density distribution,

$$\rho(r) = \frac{\rho_0}{(1+y^2)^{3\beta/2}}, \quad (2)$$

where $y = r/r_{\text{core}}$, ρ_0 , is the density at the center, and r_{core} is the scale radius for the gas distribution. The temperature of the gas was determined from the equation of hydrostatic equilibrium assuming the ideal gas equation of state with $\gamma = 5/3$. We adopted $\beta = 1$ for the large scale distribution of the intracluster gas (suggested by cosmological numerical simulations; e.g., Molnar et al. 2010).

We represented the dark matter and the stellar matter in galaxies with particles since galaxies can also be considered collisionless for our purposes. The number of particles at each AMR cell was determined by the local density, normalized according the total number of particles, which were 5 million in our simulations, assuming a gas fraction of 0.14.

The velocities of the dark matter particles were derived from sampling a Maxwellian distribution with a velocity dispersion as a function of distance from the cluster center obtained from the Jeans equation (Łokas & Mamon 2001) adopting an isotropic velocity dispersion. The direction of the velocity vectors were assumed to be isotropic (for more details on modeling the particle velocity distribution see Molnar et al. 2012).

3.2. FLASH Runs

We performed a series of numerical simulations with a total mass of $2.15 \times 10^{15} M_\odot$ and a mass ratio of 1.9 motivated by the previous analysis of El Gordo based on observations (Menanteau et al. 2012). We adopted concentration parameters of $c_1 = 8$ and $c_2 = 9$, and core radii $r_{\text{core1}} = 288 \text{ kpc}$ and $r_{\text{core2}} = 216 \text{ kpc}$, for the main and the infalling component motivated by our previous merging cluster simulations producing offsets between peaks of dark matter surface density and X-ray emission (Molnar et al. 2012). We used different impact parameters, P , and infall velocities, V_0 , searching for initial parameters which could reproduce the observed morphology of the X-ray, SZ and surface mass density of El Gordo. The initial parameters for our simulations are listed in Table 1. The IDs of our runs are listed in the first column as $RnPi jVkl$, where n is the serial number of the run, the pairs of integers, ij and kl , indicate the impact parameter, P (in units of 10 kpc),

TABLE 1
 PARAMETERS

ID ^a	V_0^b	p^c	θ^d	φ^e	D_p^f	V_r^g
R1P05V22	2250	50	48°	-60°	860	655
R2P20V22	2250	200	49°	-160°	850	690
R3P30V22	2250	300	45°	5°	914	712
R4P35V22	2250	350	44°	10°	932	745
R5P25V20	2000	250	50°	-160°	760	497
R6P25V25	2500	250	44°	10°	960	935
R7P25V30	3000	250	42°	8°	960	1376
R8P10V25	2500	100	48°	-60°	860	1000
R9P20V25	2500	200	42°	10°	960	951

NOTE. — Parameters for initial conditions (columns 2 and 3), and for snapshots shown in our figures (columns 4-7).

^a Cluster ID.

^b Infall velocity in km s^{-1} .

^c Impact parameter in kpc.

^d Polar angle of projection.

^e Roll angle of the projection.

^f Projected distance between the two dark matter peaks in kpc.

^g Radial velocity in km s^{-1} .

and the infall velocity of the run, V_0 (truncated at the 100s in km s^{-1}). The second column lists the relative initial velocities of the infalling cluster in km s^{-1} at the distance where the two clusters' truncated gas spheres touch. The third column lists the impact parameter, defined as the perpendicular distance between the trajectory of the infalling cluster and the center of the main cluster (in kpc). The other columns show parameters related to the analysis of our simulations to be discussed in Section 4.

3.3. Image Simulations

After each simulation, we generated images of the X-ray surface brightness, SZ amplitude, and total mass surface density distribution for a range of viewing angles at different phases of the collision (i.e. different output times). Our starting point for each snapshot was a coordinate system with the z coordinate axis aligned with the two dark matter centers pointing towards the infalling cluster, and the main plane of the collision (the plane determined by the two cluster centers and the relative velocity vector parallel to the z axis) aligned with the x - z plane, the x axis pointing towards the offset of the infall velocity from the main cluster center. First, we rotated the cluster around the z axis with a roll angle φ , which we changed freely, then around the x axis with a polar angle, θ , determined by the constraint of the observed projected distance between the two mass centers (active rotation: we rotated the cluster not the coordinate system). At the end, we project the cluster along the y axis, assuming that the y axis is parallel to the line of sight (LOS). In this arrangement the zero polar and roll angles ($\theta = 0$; $\varphi = 0$) mean that we assume that the collision happened in the plane of the sky.

Once we choose the time for the output and the rotation angles, we generated X-ray surface brightness images by performing a LOS integral (along the y axis) over the emissivity at fixed x and z using

$$I_X(x, z) \propto \int dy \rho_g^2 \int d\nu \varepsilon(Z_{ab}, T, \nu) A_{eff}(\nu), \quad (3)$$

where $\varepsilon(Z_{ab}, T, \nu)$ is the X-ray emissivity at frequency ν , Z_{ab} is the abundance, T is the temperature of the intracluster gas, and A_{eff} is the effective area of the telescope. We used the 4-chip averaged on axis effective area of ACIS-I (Zhao et al.

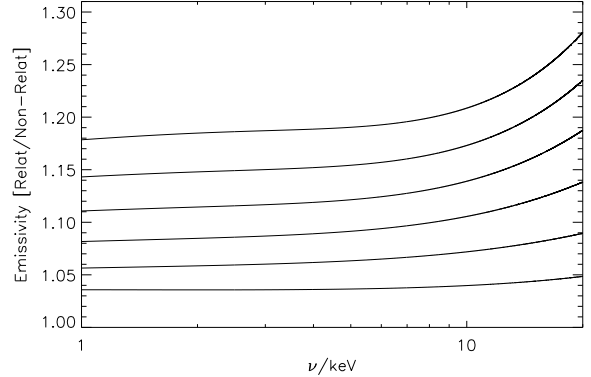


FIG. 1.— Emissivity ratios: relativistic over non-relativistic as a function of frequency (in units of keV). The lines represent emissivities at different gas temperatures: 10, 20, 30, 40, 60, 80 keV (form bottom to top).

2004) as a sufficient approximation for our purposes for comparison with the CHANDRA observations.

X-ray emission from El Gordo was detected in the 0.3–9 keV frequency band (see Figure 3 of Menanteau et al. 2012), which corresponds to 0.561–16.8 keV at emission. The compressed, shock heated gas due to merging can reach 40–80 keV at large impact velocities. At frequencies $\gtrsim 10$ keV the relativistic corrections increase the emissivity by 15–25%, as opposed to only a few percent increase at a gas temperature of 10 keV; overall, in the 0.5–17 keV frequency band, the emissivity of an 80 keV temperature gas is about 20% higher than a 10 keV gas, as it can be seen from Figure 1. In this figure we show the emissivity ratio of the relativistic to non-relativistic bremsstrahlung emissivity for gas temperatures of 10, 20, 30, 40, 60 and 80 keV as a function of frequency (in keV). Even though we are not interested in the normalization of the X-ray emission, relativistic corrections have to be included, because they change the relative normalization: they enhance the emission for high temperature gas. This enhancement is due to an increase in the relativistic Gaunt factor and the contribution from electron–electron bremsstrahlung (for a detailed discussion of the soft and hard X-ray emission due to thermal bremsstrahlung in merging galaxy clusters see Molnar et al. (2014, in preparation). However, the commonly used X-ray spectral analysis packages (e.g., Xspec⁴) have been developed for line diagnostics. The highest resolution X-ray emission package, APEC⁵ includes some corrections, but, since it has been developed for line diagnostics, does not include all corrections. Therefore we choose to calculate the continuum, $\varepsilon^C(\nu)$, and line X-ray emissivity, $\varepsilon^L(\nu)$, at frequency ν separately:

$$\varepsilon(Z_{ab}, T, \nu) d\nu = \varepsilon^C(Z_{ab}, T, \nu) + \varepsilon^L(Z_{ab}, T, \nu) d\nu, \quad (4)$$

where, for the abundance of elements, Z_{ab} , we used 30% of the Solar abundance ($Z_{ab} = 0.3Z_{\odot}$). For the continuum emissivity, we used the relativistic calculations of Nozawa et al. (1998):

$$\varepsilon^C(Z_{ab}, T, \nu) d\nu = \sum_{i=1}^N [\varepsilon_{ei}(n_e, n_i, T, \nu) + \varepsilon_{ee}(n_e, T, \nu)] d\nu, \quad (5)$$

⁴ <http://heasarc.gsfc.nasa.gov>

⁵ <http://www.atomdb.org>

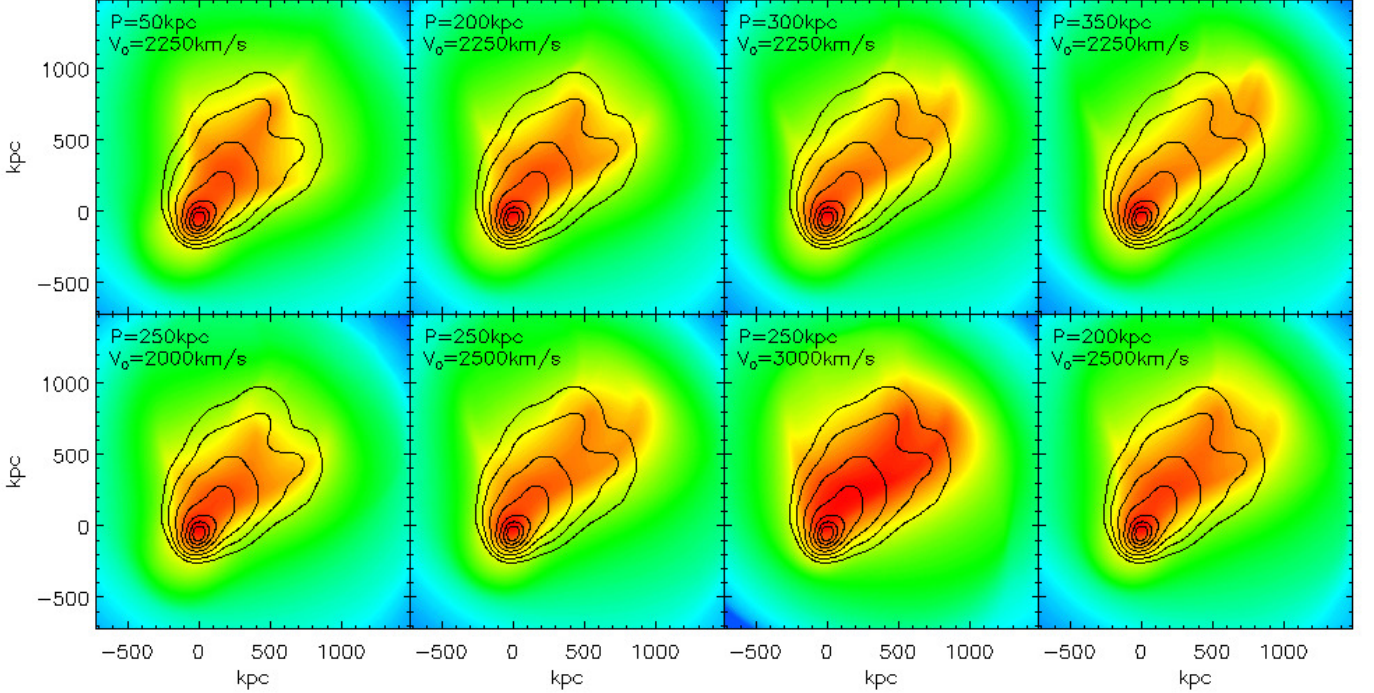


FIG. 2.— Examples of simulated X-ray surface brightness images from our merging cluster simulations with projection angles producing a cometary X-ray morphology and a wake with two tails behind the infalling cluster. In the upper row we show images from simulations with fixed infall velocity of $V_0 = 2250 \text{ km s}^{-1}$ and different impact parameters (runs R1P05V22, R2P20V22, R3P30V22, and R4P35V22; left to right). In the lower row we show images from simulations with fixed impact parameters of 250 kpc and different impact velocities, $V_0 = 2000, 2500, 3000 \text{ km s}^{-1}$, and a simulation with an impact parameter of 200 kpc and $V_0 = 2500 \text{ km s}^{-1}$ (runs R5P25V20, R6P25V25, R7P25V30 and R9P20V25; left to right). (See Table 1 for other parameters.) Contours from CHANDRA observations of El Gordo are overlaid for easier comparison (courtesy of J. P. Hughes).

where n_e and n_i are the electron and ion number densities, and the first term on the right hand side is a sum of emissivities over ions for electron–ion collisions, the second term represents the emissivity due to electron–electron collisions. The first term can be expressed as

$$\varepsilon_{ei} d\nu = c_{ep} n_e n_i Z_i^2 g(Z_i, \Theta) \Theta^{-1/2} e^{-u} d\nu, \quad (6)$$

where $c_{ep} = 16(2\pi/3)^{3/2} m_e c^2 r_e^3$, Z_i is the charge of ion i , the dimensionless temperature and frequency are $\Theta = k_B T / m_e c^2$, and $u = h_P \nu / k_B T$, where k_B and h_P are the Boltzmann and Planck constants, m_e is the mass of the electron, c is the speed of light, and the thermally averaged Gaunt factor is calculated as

$$g(Z_i, \Theta) = \frac{\pi}{8} \left(\frac{3}{2\pi} \right)^{3/2} \Theta^{7/2} e^u \frac{J^-(\Theta, u, Z_j)}{G_0^-(\Theta)}, \quad (7)$$

where r_e is the classical electron radius, $r_e = e^2 / (m_e c^2)$, (where e is the charge of the electron), and the lengthy expressions for the $J^-(\Theta, u, Z_j)$ and $G_0^-(\Theta)$ integrals, which are easily done numerically, can be found in Nozawa et al. (1998).

We used the fitting formula of Nozawa et al. (2009) for the relativistic electron–electron thermal bremsstrahlung emissivity,

$$\varepsilon_{ee} d\nu = c_{ee} n_e^2 \Theta^{-1/2} e^{-u} G_{PW}^H(\Theta, u) F_{CC}^H(\Theta, u) d\nu, \quad (8)$$

where $c_{ee} = \alpha \sigma_T m_e c^3$, where α is the fine structure constant, σ_T is the Thomson cross section, and the fitting functions $G_{PW}^H(\Theta, u)$ and $F_{CC}^H(\Theta, u)$ can be found in Nozawa et al. (2009). For the line emissivity, $\varepsilon^L(\nu)$, we used the publicly

available APEC code developed for line diagnostics⁶.

The SZ surface brightness was calculated using relativistic corrections, following Itoh, Kohyama & Nozawa (1998),

$$I_{SZ}(x, z) \propto \int dy \rho_g T_g \left[g(\nu) + \sum_{n=1}^{n=4} Y_n \Theta^n \right], \quad (9)$$

where $g(\nu) = \coth(x_\nu/2) - 4$ is the non-relativistic frequency function, where the dimensionless frequency is $x_\nu = h_P \nu / (k_B T_{cmb})$, T_{cmb} is the temperature of the cosmic microwave background, and the second term is a sum of the relativistic corrections approximated as a polynomial with coefficients, Y_n , listed in Itoh, Kohyama & Nozawa (1998).

We integrated the total (dark matter and gas) density along the y axis to generate the mass surface density images at position, x and z :

$$\Sigma(x, z) \propto \int dy (\rho_d + \rho_g), \quad (10)$$

Note that the total mass surface density maps are dominated by the main mass component, the dark matter.

4. RESULTS

When carrying out numerical simulations of binary cluster collisions, the observed mass surface density distribution provides a starting estimate for the initial masses of the two components. Although here we fix the masses to reduce the initial parameter space, they can also be determined along with other input parameters by comparing observations and numerical simulations. The observed projected distance between the

⁶ <http://www.atomdb.org>

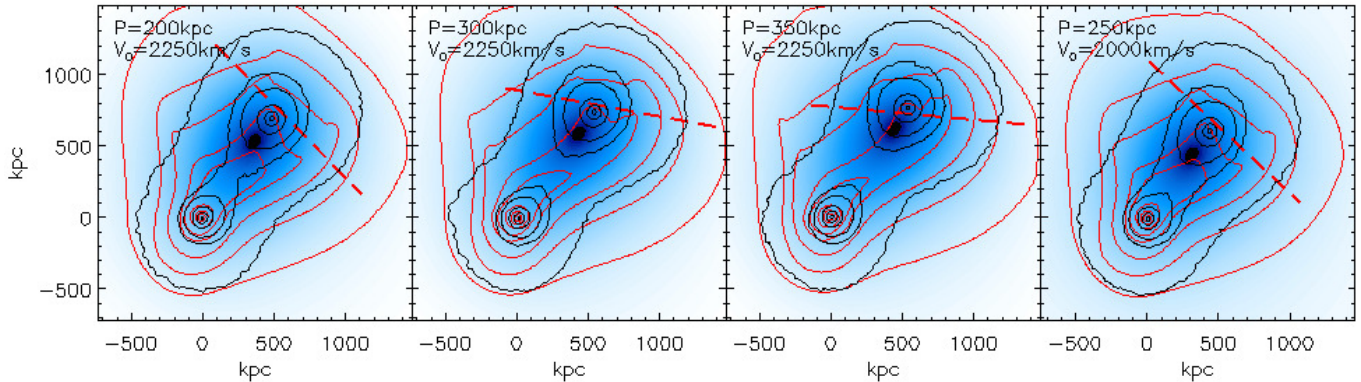


FIG. 3.— X-ray surface brightness, SZ amplitude and total mass surface density contours (red, blue, and black) from our simulations with infall velocity of $V_0 = 2250 \text{ km s}^{-1}$ and different impact parameters: $P = 200, 300, 350 \text{ kpc}$ (runs R2P20V22, R3P30V22, and R4P35V22), and from a simulation with $V_0 = 2000 \text{ km s}^{-1}$ and $P = 250 \text{ kpc}$ (run R5P25V20; left to right). Table 1 contains information of other parameters. The normalizations and contour levels are arbitrarily chosen for easy comparison with observations. The X-ray surface brightness profiles for paths shown as red dashed lines are displayed in Figure 4.

two mass centers, by itself, does not provide constraints on the phase of the collision (e.g., the time relative to the first core passage) due to possible projection effects. The phase of the collision can be constrained by using multi-frequency observations comparing the morphology of the intracluster gas derived from high resolution X-ray and/or SZ observations, and the positions of the mass centers (in projection) derived from optical/infrared observations using the method of gravitational lensing (e.g., Molnar et al. 2012). In the case of El Gordo, the SZ observations have a low angular resolution of about 1.4 (ACT). Therefore, in order to constrain the morphology of the gas, we can only use the CHANDRA X-ray observations which have a resolution of $\sim 1''$.

4.1. Reproducing the two-tail morphology

In Molnar et al. (2012) we performed a set of simulations to study the offsets between the X-ray emission, the SZ amplitude and mass surface density peaks. Based on a comparison with that study, we conclude that El Gordo is most likely after the first core passage, and before the turn around aiming for the second core passage: Before the first core passage there should have been two distinct, smooth X-ray peaks where the gas is in equilibrium around them. It must be that the core has passed for there to be only one X-ray peak and the gas has a very disturbed, cometary morphology. Therefore, in order to reduce the parameter space, we fixed the initial masses of the two components as $M_1 = 1.4 \times 10^{15} M_\odot$ and $M_2 = 7.5 \times 10^{14} M_\odot$ (mass ratio of 1.9), and ran a set of simulations changing the other parameters looking for a strongly peaked X-ray emission with a cometary structure, and two tails in the wake behind the collision after the first core passage.

We found that a series of simulations with different infall velocities $\gtrsim 2000 \text{ km s}^{-1}$ and in a relatively narrow range of impact parameters, about 200 to 350 kpc, were able to reproduce the X-ray morphology with the two tails in the wake. Simulations with small impact parameters produce three X-ray tails (see Section 5), very large impact parameters result in only one tail. In Figure 2, as an illustration, we show examples of simulated X-ray surface brightness images from our merger simulations, displayed with projection angles that match best the cometary X-ray morphology with a "twin tailed" morphology behind the infalling cluster as well as its physical size ($\sim 860 \text{ kpc}$), except the first panel in the upper row which is included for our discussion presented in Section 5 (here we ignore very faint additional tails). In this Fig-

ure we overlaid the contours from CHANDRA observations of El Gordo (Menanteau et al. 2012) for an easy comparison. In the upper row we show images from simulations with fixed infall velocity of $V_0 = 2250 \text{ km s}^{-1}$, but different impact parameters, $P = 50, 200, 300, 350 \text{ kpc}$ (runs R1P05V22, R2P20V22, R3P30V22, and R4P35V22; left to right). In the lower row we instead fix the impact parameter to 250 kpc and vary the infall velocities, $V_0 = 2000, 2500, 3000 \text{ km s}^{-1}$ (runs R5P25V20, R6P25V25, and R7P25V30; first 3 panels, left to right). The last panel in the lower row is from a simulation with $P = 200 \text{ kpc}$ and $V_0 = 2500 \text{ km s}^{-1}$ (run R9P20V25). The IDs for the runs, the infall velocities, V_0 , the impact parameters, P , and the polar and roll angles, θ and φ , of the corresponding rotations are shown in Table 1. The other two parameters shown in this table, the projected distance between the two dark matter centers and the radial velocity associated with each projection (columns 6 and 7), are discussed in Section 4.2.

We find that the phases of the collision for these massive clusters with large infall velocities ($\gtrsim 2000 \text{ km s}^{-1}$) and small mass ratios are the following: First a large scale contact discontinuity forms when the gas of the infalling cluster presses against that of the main cluster. As the infalling cluster plunges into the main cluster, adiabatically compressed layers of gas develop in both components around the contact discontinuity, and form a wedge-shaped region, and a shock develops on the two sides of the contact discontinuity. This wedge-shaped contact discontinuity passes through the main cluster and visible after the first core passage as well (upper row, first panel in Figure 2). However, in the case of El Gordo, due to an impact parameter in the order of a few hundred kpc, and a high infall velocity, only one side of the wedge-shaped region is visible in the X-ray image, because there is not enough gas on the side of the collision to produce a visible signal (e.g., first row 3rd, 4th panel in Figure 2). After the first core passage, a bow shock forms in the main cluster gas ahead of the contact discontinuity as the infalling cluster makes its way outward from the main cluster (clearly visible in all panels of Figure 2). This is the same phase as that of the Bullet cluster. At this stage of the collision, tidally stretched gas produces the X-ray emission that connects the two mass centers, seen as the Northern X-ray tail in the wake of El Gordo. This kind of tail can always be seen in simulations with smaller infall velocities, because in this case the gravitational force of the main cluster can retain enough gas to produce visible X-ray emission. In our simulated X-ray images there is a hint of

a third tail, above the tidally stretched gas, which is due to the compressed gas on that side of the collision axis. The X-ray emission observed in El Gordo suggests the presence of a possible third tail, indicated by enhanced emission to the North-West of the X-ray peak. However, the photon counts are quite low in this direction. Our simulations suggest that a third X-ray tail above the two observed tails would be visible in an X-ray image of El Gordo with a longer exposure time.

4.2. Reproducing projected distance and relative radial velocity

We have demonstrated that the observed cometary X-ray morphology and system size of El Gordo can be reproduced by our simulations using several infall velocities and impact parameters values (Figure 2). As a next step, we use the observed projected distance between the two dark matter centers and the observed relative radial velocity of the infalling cluster to constrain the initial parameters of the system. The mass center of the main (NW) component marked by the rest frame i -band and $3.6 \mu\text{m}$ luminosity density, stellar mass density (Menanteau et al. 2012), and mass surface density derived from gravitational lensing (Jee et al. 2013) are all very close to each other, so they seem to be reliable. On the other hand, the position of the mass peak of the infalling cluster, the SE component, derived using different methods show about a 170 kpc scatter around the X-ray peak. Since our simulations suggest that the X-ray peak and the mass peak of the infalling cluster should be close, we adopt the position of the X-ray peak as the center of the infalling cluster. Thus we demand that the projected distance between the centers of the two components in our merging simulations to be ~ 860 kpc. Based on galaxy redshift measurements, the observed relative radial (LOS) velocity between the infalling cluster center and the main component was found to be $586 \pm 96 \text{ km s}^{-1}$ (Menanteau et al. 2012). However, the observed radial velocity of the BCG was $731 \pm 66 \text{ km s}^{-1}$, so we may assume that the radial relative velocity in El Gordo falls in the interval of $500\text{--}800 \text{ km s}^{-1}$.

The projected distances between the mass centers and the relative radial velocities for our simulations are listed in Table 1 (columns 6 and 7). Based on this table, we conclude, that simulations with an infall velocity of $V_0 = 2250 \text{ km s}^{-1}$ and impact parameters $P = 200, 300,$ and 350 kpc (runs R2P20V22, R3P30V22, and R4P35V22), and $V_0 = 2000 \text{ km s}^{-1}$ and $P = 250$ kpc (run R5P25V20) provide a good match with the X-ray morphology, the positions of the X-ray peak and mass peaks, and the constraints from the observed radial relative velocity. We can exclude run R1P05V22, because it has three tails due to the small impact parameter of $P = 50$ kpc (we included only for comparison with the simulation carried out by Donnert 2014 for El Gordo). In general we can exclude simulations with small impact parameters because they produce either one or three tails depending on the infall velocities. Runs R6P25V25, R7P25V30, and R9P20V25 can be excluded as well, because these simulations with larger infall velocities produce either too large projected distances between the two mass centers, or too large radial velocities. In Figure 3 we show the X-ray surface brightness, SZ and mass surface density contours for these simulations (runs R2P20V22, R3P30V22, R4P35V22, and R5P25V20) in the same projection as in Figure 2 (see Table 1 for the parameters). All four contour images show similar morphology. The X-ray and mass contours show that the mass centers of the “bullet” coincide with the X-ray peak. At these assumed infall velocities,

unlike in the case of the Bullet cluster, the ram pressure is not sufficient to drag the gas behind the dark matter component as it passes through the main cluster gas cloud. Thus our simulations predict that we will not find an offset between the X-ray peak and the mass center of the “bullet” using more precise observations. On each image, the mass center of the main cluster is located at the North-Western end of the Northern tail, as predicted by observations.

4.3. Reproducing the X-ray brightness profile

We further constrain the infall velocity and the impact parameter of the collision for El Gordo comparing the shapes of our X-ray surface brightness profiles across the wake with that from CHANDRA observations (Figure 1 of Menanteau et al. 2012). The observed profile is nearly symmetric with two maxima separated by about $35''$, and a local minimum between them. First, we went through different snapshots for each run after the first core passage with a separation between the two dark matter centers of $600\text{--}1200$ kpc, and generated X-ray images by projecting them out with a set of different polar and roll angles on a grid, and kept those snapshots and projections which resembled El Gordo (showed a cometary morphology with one peak X-ray emission and two tails in the wake of the infalling cluster). As a next step, we extracted X-ray surface brightness profiles along cuts through the wake with different positions and rotation angles, and found the best fits to the CHANDRA data. The extracted X-ray surface brightness profiles of those projections of each run that produced the best match with El Gordo observations are shown in Figure 4 (runs R2P20V22, R3P30V22, R4P35V22, and R5P25V20). The X-ray images for these snapshots with the same projections are shown in Figure 2 (upper row panels 2, 3 and 4, and lower row first panel). The corresponding paths are displayed in Figure 3 (red dashed lines). In Figure 4 the El Gordo observations are also shown with points with error bars (read off from Figure 1 of Menanteau et al. 2012). Our simulation with $V_0 = 2250 \text{ km s}^{-1}$, and $P = 300$ kpc is the best match with the observed profile. Our simulation with $V_0 = 2250 \text{ km s}^{-1}$ and a smaller impact parameter, $P = 200$ kpc, and a simulation with $V_0 = 2000 \text{ km s}^{-1}$ and $P = 250$ kpc (runs R2P20V22 and R5P25V20) have the two peaks too far from each other, the profile from our simulation with $V_0 = 2250 \text{ km s}^{-1}$ and larger impact parameter, $P = 350 \text{ km s}^{-1}$ (run R4P35V22) has three X-ray peaks in the wake. Therefore, based on the observed X-ray morphology, the profile of the X-ray surface density across the wake, the relative radial velocity, and the relative positions of the X-ray, SZ and mass peaks, subject to the limitations of our models, we derive an infall velocity of $V_0 = 2250 \pm 250 \text{ km s}^{-1}$, and a large impact parameter of $P = 300^{+50}_{-100}$ kpc for El Gordo (note, the errors shown are rough estimates only).

5. DISCUSSION

Our results confirm the basic interpretation of the merging cluster El Gordo by Menanteau et al. (2012): this system is after the first core passage of a large infall velocity collision, the infalling cluster moving from the NW towards SE, and the main cluster center coincides with the observed position of the mass concentration of the NW component. Based on the merger morphology, Menanteau et al. (2012) proposed that the inclination angle (between the collision axis and the plane of the sky) should be shallow. Assuming that the infall velocity is close to the velocity of the observation after

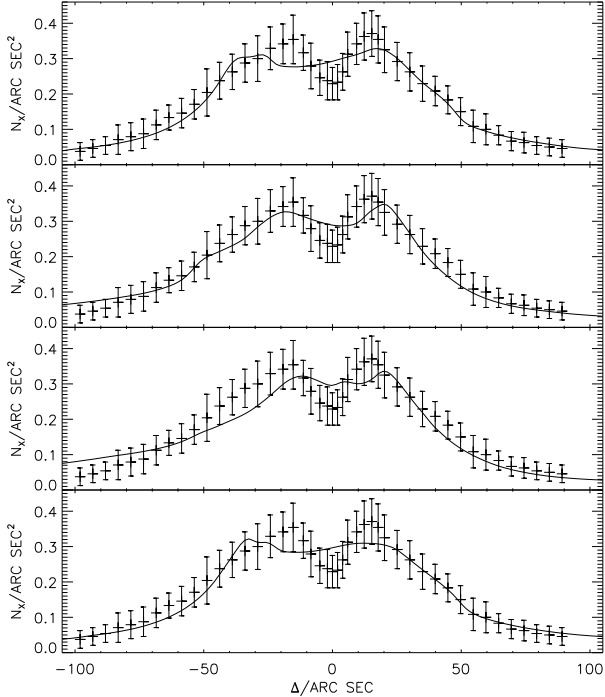


FIG. 4.— Time integrated X-ray surface brightness (in photon counts, N_X , per arc sec²) across the wake of the cluster merger taken from the Chandra observations (data points with error bars) overlaid on those extracted from our FLASH simulation (solid lines). The simulations were done with an infall velocity of $V_0 = 2250$ km s⁻¹ and different impact parameters, $P = 200, 300, 350$ kpc (runs R2P20V22, R3P30V22, and R4P35V22) and with $V_0 = 2000$ km s⁻¹ and $P = 250$ kpc (run R5P25V20) as a function of distance along the path, Δ , in arc second (top to bottom). The same projections of these simulations are shown in Figure 3. The extraction path for these profiles (shown as red dashed lines in Figure 3) were chosen to provide the best match with the X-ray surface brightness profile across the wake of El Gordo derived from CHANDRA observations.

the first core passage, Menanteau et al. predicted an infall velocity of 2300 km s⁻¹ and 1200 km s⁻¹ for polar angles of 15° and 30°. Our best result with an infall velocity of 2250 km s⁻¹ (run R4P35V22) is in a good agreement with their prediction, however this is a coincidence. The relative velocity of this run at the phase of best fit with observations is 1009 km s⁻¹. This shows that the instantaneous velocity at a phase after the first core passage could be 50% of the infall velocity (or it could even be zero at the phase of the turnaround). The rotation angle out of the sky (the main plane of the collision), i.e., the polar angle, θ , in our case is 45°. Following Menanteau et al.’s procedure, using this rotation angle, we would find $600/\sin 45^\circ \approx 850$ km s⁻¹ for the infall velocity, and not 2250 km s⁻¹.

Donnert (2014) carried out simulations to reproduce the observed properties of El Gordo. Most of the important initial conditions adopted were similar to ours (we also based our simulations on the results of Menanteau et al. 2012): large masses and the core radius for the main component: $M_1 = 1.9 \times 10^{15} M_\odot$, $M_2 = 8.1 \times 10^{14} M_\odot$, $r_{core1} = 300$ kpc, infall velocity: 2600 km s⁻¹. However, the impact parameter, the concentration parameters, β , and the core radius of the infalling cluster were significantly smaller than ours: 20 kpc, $c_1 = 2.9$, $c_2 = 3.2$, $\beta = 2/3$, $r_{core2} = 25$ kpc, as well as $\beta = 2/3$, and the initial distance, which does not affect the results, larger: 5231 kpc.

Donnert used a Hernquist profile (Hernquist 1990) for the

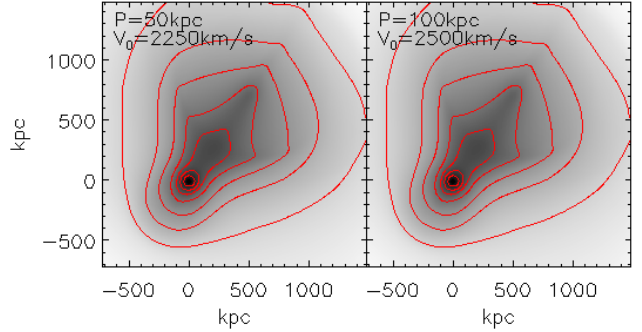


FIG. 5.— X-ray surface brightness images from our FLASH simulations with small impact parameters, $P = 50$ and 100 kpc, and infall velocities of $V_0 = 2250$ and 2500 km s⁻¹ (runs R1P05V22 and R8P10V25; left to right). For other parameters see Table 1. The contours of the same data are overlaid to emphasize the morphology.

distribution of dark matter without a cut off at the virial radius, but since the density profile of this model falls off as r^{-4} , the density is quite low at large radii, whereas we used a truncated NFW profile with zero density at large radii. This difference should not have any significant effect on neither the dynamics of the collision nor the observable X-ray emission around the first core passage. Donnert’s simulations reproduced the X-ray luminosity of El Gordo, the distances between peaks of the X-ray emission, SZ signal and the mass surface density well. However, the X-ray morphology was not reproduced correctly: the cometary structure showed only one tail pointing to the center of the mass distribution of the main cluster. Our simulations were able to reproduce the two X-ray tails with a range of infall velocities (2000–3000 km s⁻¹) and impact parameters (200–350 kpc).

Turbulence plays an important role in structure formation, it facilitates the mixing of the intracluster gas during cluster merging. Comparisons between SPH and Eulerian AMR codes suggest that artificial viscosity, necessary in SPH codes to handle shocks, suppress dynamical instabilities, and thus turbulent mixing of the gas (Mitchell et al. 2009; Agertz et al. 2007). Therefore, as opposed to Donnert, we chose to use an AMR code for our merging cluster simulations. However, the main physical process which produces ordered large scale shock-heated and compressed gas is more likely linked to formation of contact discontinuities and not to turbulence.

In Figure 5 we show X-ray images from our merging cluster simulations with an infall velocity of $V_0 = 2250$ km s⁻¹ and an impact parameter of $P = 50$ kpc, and with $V_0 = 2500$ km s⁻¹ and $P = 100$ kpc (runs R1P05V22 and R8P10V25; left to right). We overlaid the contours of the same X-ray images to emphasize the morphology. These images show a similar symmetric morphology to that of Donnert, who used $V_0 = 2600$ km s⁻¹ and $P = 20$ kpc. We may conclude that even an impact parameter of 50 or 100 kpc would not break the symmetry of the X-ray images significantly, and can not produce the asymmetric two-tail morphology of El Gordo. In both of these panels of Figure 5, three tails can be seen, a larger tail in the middle and two fainter tails in a wedge shape pointing towards the bullet. Our simulations suggest that the one tail seen in the wake of Donnert’s simulation is due to the tidally stretched gas between the two mass centers. A similar wedge-shaped structure is generated in Donnert’s simulation, but it disappears after the first core passage (Figure 5 of Donnert 2014). We speculate that Donnert’s simulation with a small impact parameter produced only one X-ray tail and not three since

they assumed the infalling cluster is in a bubble inside the main cluster atmosphere. This causes their contact discontinuity to form only between the two cores and not on a large scale of the entire cluster, as in our simulations (Molnar et al. 2013a, 2012). In our simulations, we needed impact parameters of a few 100 kpc to produce two asymmetric X-ray tails. We note that our simulation, R8P10V25, with the same infall velocity, 2500 km s^{-1} , used by Donnert and with a small impact parameter, predicts a relative radial velocity of 1000 km s^{-1} , much larger than observed (Table 1).

6. CONCLUSIONS

Using self-consistent N-body/hydrodynamical simulations we confirm the previous interpretation of El Gordo, as a massive galaxy cluster in an early stage of merging, about 480 million years after a first core passage, well before the first turn around. We have used the X-ray morphology, SZ, gravitational lensing and radio observations of El Gordo to constrain the initial conditions of this merging system. We have found that our simulations within a relatively narrow range of infall velocities and impact parameters can reproduce the data well. In particular, we can reproduce the distinctive “twin-tailed” cometary X-ray morphology of El Gordo with a simple clear physical explanation. We match the observations with an initial infall velocity of $\simeq 2250 \text{ km s}^{-1}$, when the clusters are separated by the sum of their virial radii. The impact parameter of the collision is well constrained at $\simeq 300 \text{ kpc}$ to provide the asymmetric second tail which is a projection of the compressed and shock heated gas front. We quantify this using the profile of the X-ray surface brightness across the wake (Menanteau et al. 2010), by the relative radial velocity from spectroscopy of member galaxies, and from the relative positions of the X-ray, SZ and mass peaks. Note that our best simulation does reconstruct all the observed morphological features of El Gordo, as well as the X-ray surface brightness across the wake quantitatively, but the position of the extraction region through the wake is not an exact match with that of the CHANDRA observations. Therefore, for a more accurate determination of the infall velocity, we need to perform

a search in a larger parameter space including the masses of the components, their concentration parameters, core radii for the intracluster gas. This task necessitates many more simulations, which we defer to a future study.

This massive merging cluster with an infall velocity of 2250 km s^{-1} at the time the Universe was half of its age (at the redshift of $z = 0.87$) is apparently very unusual in the standard Λ CDM models, for which extensive simulations have been performed to determine the expected probability distribution of relative velocities (Thompson & Nagamine 2012). At face value, such extreme cases present a challenge to our understanding of structure formation and may lead to a better understanding of dark matter and/or alternative theories of gravity. We aim to expand our grid of input parameters for a fuller investigation of the uniqueness of our solution and the uncertainties on the derived physical parameters using more powerful GPU accelerated architectures. We will also benefit from deeper X-ray observations and higher resolution SZ imaging to more accurately constrain our models. This work will become increasingly more important for cosmology as new discoveries of extreme cluster collisions are uncovered in the new wide area SZ surveys sensitive to high pressure shocked gas and also from future radio surveys sensitive to “relic” radio emission from merger shocks.

The code FLASH used in this work was in part developed by the DOE-supported ASC/Alliance Center for Astrophysical Thermonuclear Flashes at the University of Chicago. We thank the Theoretical Institute for Advanced Research in Astrophysics, Academia Sinica, for allowing us to use its high performance computer facility for our simulations. We thank J. P. Hughes for providing us the processed X-ray data from their CHANDRA observations of El Gordo, and the referee for a thorough reading of our paper and for suggestions, which helped to improve on the presentation of our results. This research has made use of the NASA/IPAC Extragalactic Database (NED) which is operated by the Jet Propulsion Laboratory, California Institute of Technology, under contract with the National Aeronautics and Space Administration.

REFERENCES

- Agertz, O., Moore, B., Stadel, J., et al. 2007, MNRAS, 380, 963
 Bourdin, H., Arnaud, M., Mazzotta, P., et al. 2011, A&A, 527, A21
 Bradač, M., Allen, S. W., Treu, T., et al. 2008, ApJ, 687, 959
 Dawson, W. A., Wittman, D., Jee, M. J., et al. 2012, ApJ, 747, L42
 Donnert, J. M. F. 2014, MNRAS, 438, 1971
 Fryxell, B., et al. 2000, ApJS, 131, 273
 Gastaldello, F., Limousin, M., Föex, G., et al. 2014, arXiv:1404.5633
 Hayashi, E., & White, S. D. M. 2006, MNRAS, 370, L38
 Hernquist, L. 1990, ApJ, 356, 359
 Itoh, N., Kohyama, Y., & Nozawa, S. 1998, ApJ, 502, 7
 Jee, M. J., Hughes, J. P., Menanteau, F., et al. 2013, arXiv:1309.5097
 Komatsu, E., Dunkley, J., Nolta, M. R., et al. 2009, ApJS, 180, 330
 Korngut, P. M., Dicker, S. R., Reese, E. D., et al. 2011, ApJ, 734, 10
 Lee, J., & Komatsu, E. 2010, ApJ, 718, 60
 Lindner, R. R., Baker, A. J., Hughes, J. P., et al. 2014, ApJ, 786, 49
 Łokas, E. L., & Mamon, G. A. 2001, MNRAS, 321, 155
 Markevitch, M., Gonzalez, A. H., Clowe, D., et al. 2004, ApJ, 606, 819
 Markevitch, M., Gonzalez, A. H., David, L., et al. 2002, ApJ, 567, L27
 Massardi, M., Ekers, R. D., Ellis, S. C., & Maughan, B. 2010, ApJ, 718, L23
 Mastroiello, C., & Burkert, A. 2008, MNRAS, 389, 967
 Menanteau, F., Hughes, J. P., Sifón, C., et al. 2012, ApJ, 748, 7
 Menanteau, F., et al. 2010, ApJ, 723, 1523
 Mitchell, N. L., McCarthy, I. G., Bower, R. G., Theuns, T., & Crain, R. A. 2009, MNRAS, 395, 180
 Molnar, S. M., Chiu, I.-N. T., Broadhurst, T., & Stadel, J. G. 2013, ApJ, 779, 63
 Molnar, S. M., Broadhurst, T., Umetsu, K., et al. 2013, ApJ, 774, 70
 Molnar, S. M., Hearn, N. C., & Stadel, J. G. 2012, ApJ, 748, 45
 Molnar, S. M., et al. 2010, ApJ, 723, 1272
 Molnar, S. M., Hearn, N., Haiman, Z., et al. 2009, ApJ, 696, 1640
 Mortonson, M. J., Hu, W., & Huterer, D. 2011, Phys. Rev. D, 83, 023015
 Mroczkowski, T., et al. 2012, in press, arXiv:1205.0052
 Navarro, J. F., Frenk, C. S., & White, S. D. M. 1997, ApJ, 490, 493
 Nozawa, S., Takahashi, K., Kohyama, Y., & Itoh, N. 2009, A&A, 499, 661
 Nozawa, S., Itoh, N., & Kohyama, Y. 1998, ApJ, 507, 530
 Owers, M. S., Couch, W. J., Nulsen, P. E. J., & Randall, S. W. 2012, ApJ, 750, L23
 Ricker, P. M. 2008, ApJS, 176, 293
 Russel, h. R., et al. 2010, arXiv:1004.1559
 Sayers, J., Mroczkowski, T., Zemcov, M., et al. 2013, ApJ, 778, 52
 Springel, V., & Farrar, G. R. 2007, MNRAS, 380, 911
 Thompson, R., & Nagamine, K. 2012, MNRAS, 419, 3560
 Watson, W. A., Iliev, I. T., Diego, J. M., et al. 2014, MNRAS, 437, 3776
 Zhao, P., et al., 2004, in “X-Ray and Gamma-Ray Telescopes and Instruments for Astronomy XIII”, eds.: Flanagan, Kathryn A. and Siegmund, Oswald H. W., Proceedings of SPIE Vol. 5165, p. 482
 Zitrin, M. J., Menanteau, F., Hughes, J. P. et al. 2013, arXiv:1304.0455